PAPER • OPEN ACCESS

A methodical approach to design adiabatic waveguide couplers for heterogeneous integrated photonics

Journal of Physics: Photonics

PAPER

A methodical approach to design adiabatic waveguide couplers for heterogeneous integrated photonics

Jef Van Asch[1,2,5,*], Ahmed Kandeel[1,3,5,*], Junwen He[1,4], Jeroen Missinne[2], Peter Bienstman[3], Dries Van Thourhout[3], Geert Van Steenberge[2] and Joris Van Campenhout[1]

[1] Imec, Kapeldreef 75, 3001, Leuven, Belgium
[2] Centre for Microsystems Technology (CMST), imec and Ghent University, Technologiepark 126, 9052 Gent, Belgium
[3] Photonics Research Group (PRG), imec and Ghent University, Technologiepark 126, 9052 Gent, Belgium
[4] Currently at Huawei Technologies
[5] These authors contributed equally to this work.
[*] Authors to whom any correspondence should be addressed.

E-mail: jef.vanasch@imec.be and ahmed.kandeel@imec.be

Keywords: photonic integrated circuits, heterogeneous integration, adiabatic coupling, optical design, 'Mono' taper

OPEN ACCESS

RECEIVED
26 April 2024

REVISED
26 August 2024

ACCEPTED FOR PUBLICATION
18 September 2024

PUBLISHED
27 September 2024

Abstract

We present an elegant and effective approach for the design of adiabatic waveguide couplers tailored for the heterogeneous integration of photonic building blocks. This method empowers users to incorporate the shortest taper(s) in their designs, while upholding optimal coupling efficiency. The technique assesses mode overlap between a minimum of two waveguides within the cross-section of any heterogeneous material stack, determining the necessary waveguide cross-sectional dimension to achieve optimal coupling efficiency. Two illustrative design applications are showcased and compared to a linear, concave, and convex taper for reference: a SiN-to-polymer structure exhibiting a 40% coupling improvement and a Si-to-GeSi structure having a 2.2 up to 5 times shorter length.

1. Introduction

Silicon photonics has emerged over the last decade as a promising solution for future applications such as high-speed optical interconnects for 5G fronthaul, industrial automation, self-driving cars, datacenter, computer-memory disaggregation and beyond [1]. By leveraging the complementary metal–oxide–semi conductor (CMOS) fabrication technology developed previously for the electronics industry, various high-speed active optical components such as modulators and photodetectors have been developed [2, 3]. Moreover, the production methods for passive optical components such as grating couplers [4], and waveguides [5] have been optimized in various fabs. To further enhance the optical connection between passive and active components on and coupling from/to a photonic integrated circuit (PIC), the proper design and shape of the interconnecting waveguides plays a crucial role. With the introduction of new photonic building blocks, such as the heterogeneous integration of III–V light sources on a silicon chip, continuous improvement is required.

There are three common approaches to achieve light coupling between two waveguides: butt coupling, directional coupling, and adiabatic coupling. The butt coupling approach refers to the mode profile matching of two waveguides, directly connected to each other. Its coupling efficiency is optimized by maximizing the mode field overlap. Consequently, for heterogeneous integration, in which light needs to be coupled between different components on top of each other, butt coupling is not the preferred option. In the directional coupling approach, light is coupled between two parallel waveguides when the mode at the input waveguide is coupled into a superposition of supermodes at the coupling region. The mode is periodically completely coupled from one waveguide to the other at half beat length and the beat length could be designed to be short [6]. However, the exact beat length is difficult to precisely determine in practice, making the power transfer efficiency and the device performance uncertain. Additionally, directional couplers have a limited bandwidth since the beat length is wavelength dependent. In the adiabatic coupling approach, the

optical mode is coupled from one waveguide to another due to a slow change of a waveguide parameter (width, thickness, or both), such that the optical mode remains in the fundamental mode and does not couple to unwanted higher order modes. As a result, the tapered waveguides need to be long enough to meet the requirements of the adiabatic conditions of slow change of waveguide parameter, but at the same time they need to meet the device compactness requirement. Hence, a trade-off is required. Since the adiabatic couplers do not depend on interference, the corresponding bandwidth is large, and they are more robust against fabrication tolerances. In [7], a directional coupler and adiabatic coupler design methodology is proposed for coupling light between a III–V laser and a Si waveguide. Although the directional coupler showed good coupling efficiency, it had a poor performance against fabrication tolerance and temperature variations. For that reason [7], proposed an adiabatic coupler design to mitigate these drawbacks of the directional coupler. Similarly, the potential use of adiabatic couplers for heterogeneous structures was demonstrated in [8], stressing the need for a user-friendly taper design method.

There are different efforts that have been made to present design methods for designing adiabatic mode couplers [9–19]. For example [9], proposes a design concept for a mode adapter in which a 'single-step loss' is used. However, the method is mainly used for mode conversion within the same waveguide material. To couple light from one waveguide to another, the current adiabaticity methods rely on the coupling of (one of) the supermodes. The maximum allowed loss can be derived by amplitude $|a_e|$ and/or $|a_o|$ (even/odd supermode) as the electric field in the mode transformer can be expressed as linear combination of the supermodes [10]. The eventual relation between the taper propagation length and width is fundamentally derived starting from the Fresnel equation and/or coupled local-mode theory [11]. These methods require prior knowledge of the existing supermodes.

In this paper, we propose a new method that does not rely on the decomposition of supermodes at the start and end of the taper but considers the overlap integral of the supermode(s) present in the current cross-section with the ones present in a slightly altered cross-section. Therefore, the transmission of the supermodes is monitored throughout the entire taper structure. This monotonic ('Mono') mode tracking approach gives insight into the supermodes' evolution along the tapered waveguide. Comparing our method to currently existing ones, the main advantage is the method's simplicity for the designer to calculate the mode transformation in complex heterogeneous structures. Given the heterogeneous setup's cross-section, the fast 2D simulation results display the optimized taper shape that is concentrated around the phase-matching point. This significantly reduces the taper length and still offers the designer the flexibility to focus on the preferred (TE/TM) polarization. Additionally, the method allows more than two waveguides to be present in the cross-section, for example allowing the coupling from one waveguide to a *Y*-shape waveguide.

2. Methods and materials

While propagating through the taper, the supermode's evolution is characterized by a power coupling loss $\mathrm{d}\gamma$ caused by a variation in width $\mathrm{d}W$. This infinitesimal coupling mismatch is strongly determined by the current stack of materials in close optical proximity of the waveguide, each having their own specific dimensions and refractive index values. Assuming that all dimensions are constant except the tapering waveguide width W, $\mathrm{d}\gamma$ is heavily dependent on (the change of) the current waveguide width $\mathrm{d}W$ and W, as shown in figure 1. Therefore, $\mathrm{d}\gamma$ can be deduced as a multiplication of dW and a W-dependent factor α that we call the local adiabaticity parameter

$$\mathrm{d}\gamma = \alpha(W)\ \mathrm{d}W. \tag{1}$$

Analyzing the power coupling efficiency along the propagation direction z, leads to the following equations:

$$\frac{\mathrm{d}\gamma}{\mathrm{d}z} = \alpha(W)\frac{\mathrm{d}W}{\mathrm{d}z} = \varepsilon. \tag{2}$$

Herein, we rely on the adiabaticity criterion [11] to state that the change in local adiabaticity $\alpha(W)$ with respect to z is much smaller than the change in width W. Additionally, it is assumed that the local change of γ with respect to z is constant and equal to a parameter ε [10]. Defining W_1 and W_2 as the start and end width of the complete taper, with z_1 and z_2 the start and end z-coordinate along the propagation direction, this leads to the following equation,

$$z_2 - z_1 = \frac{1}{\varepsilon}\int_{W_1}^{W_2} \alpha(W)\,\mathrm{d}W. \tag{3}$$

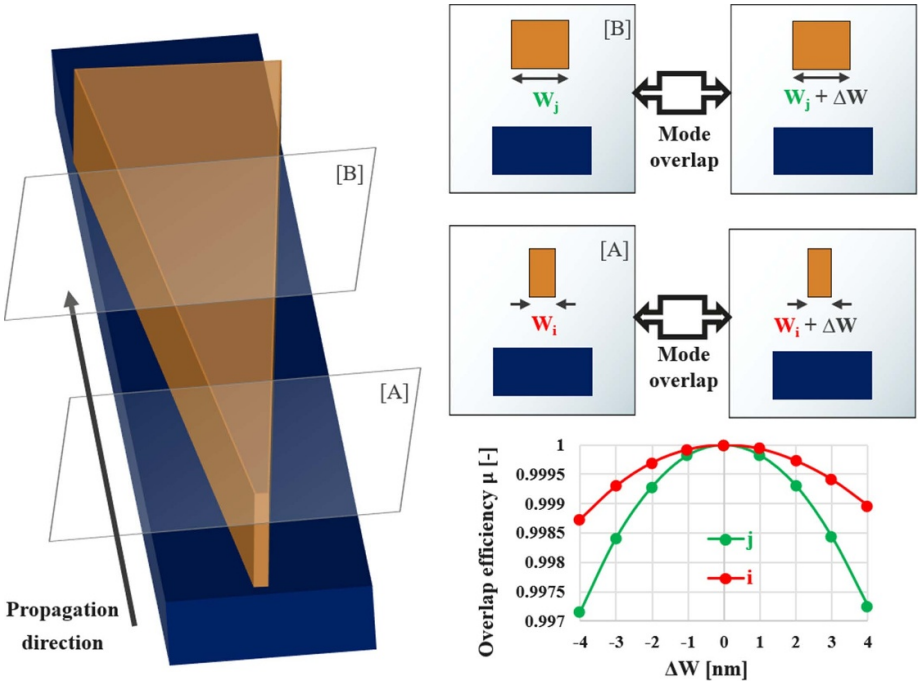

Figure 1. Graphical illustration how the width of an arbitrary waveguide determines the mode overlap between the current width W and a slightly increased width W+ΔW.

The local adiabaticity $\alpha(W)$ is an instantaneous taper parameter that depends on the width at each cross section and characterizes the sensitivity of any width variation. For widths close to the phase matching point, any abrupt change in width W results in high coupling loss dγ and thus a large value for the local adiabaticity $\alpha(W)$. For widths W farther away from the phase matching condition, the sensitivity is lower, hence $\alpha(W)$ is low as well. The exact form for $\alpha(W)$ can be found by looking at the mode overlap between two modes; the first mode is the one at each considered cross section along the taper at a certain width W_i (with $W_1 \leqslant W_i \leqslant W_2$ when tapering up and $W_1 \geqslant W_i \geqslant W_2$ when tapering down), and the second mode is the one which corresponds to the width $W_i + \Delta W$. We define that W_i ranges from W_1 up to W_2 with steps of 10 nm or smaller, while ΔW ranges from -4 nm up to 4 nm with steps of 1 nm. Hence, for each cross-section width W_i, the corresponding $\alpha(W_i)$ is obtained by calculating the overlap interval with its 9 closest altered cross sections $W_i + \Delta W$. The mode overlap calculations are performed using Ansys Lumerical finite-difference eigenmode (FDE) solver based on the following equation [20],

$$\text{overlap efficiency } \mu \equiv Re\left[\frac{\left(\int \overrightarrow{E_I} \times \overrightarrow{H_{II}^*} \cdot \mathrm{d}\vec{S}\right)\left(\int \overrightarrow{E_{II}} \times \overrightarrow{H_I^*} \cdot \mathrm{d}\vec{S}\right)}{\left(\int \overrightarrow{E_I} \times \overrightarrow{H_I^*} \cdot \mathrm{d}\vec{S}\right)\left(\int \overrightarrow{E_{II}} \times \overrightarrow{H_{II}^*} \cdot \mathrm{d}\vec{S}\right)}\right]. \tag{4}$$

This is the overlap integral between the two modes, where the electric and magnetic field E and H with index values I resp. II correspond to width W_i and $W_i + \Delta W$. The overlap calculations in figure 1 are for different cross sections with width W_i and W_j. The calculations show the drop in overlap efficiency μ for discrete ΔW values, as well as the W-dependency (depicted by the different concavity). For example, we can see in this example that the cross section with width W_j shows higher concavity than the case for W_i, so this means that the cross section of W_j is more sensitive for variation compared to the case of W_i. The quasi-symmetric behaviour of $\mu(W)$ allows us to use a Gaussian profile to fit the simulated results:

$$\mu(W) \equiv \exp\left(-\frac{(\Delta W)^2}{(C(W))^2}\right). \tag{5}$$

The purpose of this fitting function is to extract the parameter C for each cross section, which is directly related to the concavity of the Gaussian function. It is inversely proportional to the rate of change (or concavity) of the function. Since each cross section, thus each W_i, will have a different overlap function, the C parameter is also a W-dependent function specific for each guided mode as defined in equation (5). As will be shown later in figure 4, its dependency on W is characterized by a local minimum where the phase matching condition is optimal between both (tapered) waveguides.

Coming back to equation (2), the local adiabaticity $\alpha(W)$ can now be linked to the C(W) behaviour. After performing many simulations for the most optimal equation, we empirically state that $\alpha(W)$ and $C(W)$ are inversely related:

$$\alpha(W) = \frac{1}{C(W)}. \tag{6}$$

Intrinsically this makes a lot of sense: For W-values where the $C(W)$ reaches its lowest values, the resulting coupling is highest, hence $\alpha(W)$ is highest. Consequently, the width increment dW needs to be small to maintain the same loss throughout the entire taper. Note that $C(W)$ is polarization dependent as it is specifically linked to a guided mode. Therefore, when optimizing the taper shape, a trade-off needs to be made which polarization is most suitable to rely on for choosing the $\alpha(W)$ behaviour. For applications in which TE/TM polarizations are mode converted by hybridization (such as polarization rotators), we refer to literature on how to modify the configuration [21]. Combining equations (3) and (6), we obtain the following formula for the total adiabatic taper shape, for a waveguide width ranging from W_1 up to W_2:

$$z_2 - z_1 = \frac{1}{\varepsilon}\int_{W_1}^{W_2} \frac{1}{C(W)}\mathrm{d}W. \tag{7}$$

Finally, we can deduce the more general taper profile based on previous equations. If we claim $z_1 = z(W_1) = 0$ at the start of the taper, the relation between propagation distance z and waveguide width W can be written as follows:

$$z(W) = \frac{1}{\varepsilon}\int_{W_1}^{W} \frac{1}{C(W')}\mathrm{d}W'. \tag{8}$$

This formula allows to accurately define the taper shape for one or both waveguides to obtain the highest coupling efficiency based on one variable W. All other relevant parameters (such as refractive index values, waveguide heights, inter-waveguide distance, …) are included in corresponding $C(W)$ functions, outputted by the FDE simulations. For any desired optical configuration, given the corresponding refractive indices for all used materials, only one parameter sweep must be calculated to obtain the optimal taper design as the final outcome.

The next sections of this paper illustrate two practical use cases to apply this 'Mono' theory. One example discusses a SiN-to-polymer coupling structure, in which only the SiN waveguide is tapered. The other example showcases adiabatic coupling between Si and GeSi by tapering both waveguides in opposite direction.

3. Results and discussion

3.1. SiN to polymer coupling: single taper

As a first showcase, we consider an O-band configuration to support Co-Packaged Optics (CPO), as demonstrated experimentally in [22]. In the setup, light is coupled between a SiN tapered waveguide and a polymer waveguide. As depicted in figure 2, the SiN waveguide has a thickness of 400 nm and is tapered down in width from initially 710 nm until 130 nm at the taper tip. The polymer waveguide's dimensions are chosen to obtain a first order, circular mode profile, i.e. having a thickness of 5.7 μm and width of 4.0 μm [23]. At $\lambda = 1310$ nm, the polymer core's refractive index value is 1.579, while its surrounding polymer cladding has a refractive index equal to 1.571. These are values corresponding to the commercially available EpoCore/EpoClad material [24]. Finally, the refractive index values for SiN, BCB and SiO_2 are respectively 2.0, 1.537 and 1.44 at $\lambda = 1310$ nm.

As previously discussed, the coupling loss γ is predominantly influenced by the overlap efficiency $\mu(W)$ at each cross-section with waveguide width W. The higher the overlap efficiency for all investigated waveguide widths, the lower the total coupling loss γ. Figure 3 graphically presents the behavior of the fundamental TE mode for specific discrete values of W, obtained through Lumerical Mode FDE simulations. For clarity, only the fundamental TE mode is depicted, but the same analysis is valid for the fundamental TM mode. As anticipated, the Gaussian fit provides a reliable approximation to the experimental data points.

Upon narrowing the SiN waveguide, it becomes evident that the overlap diminishes rapidly when the waveguide width approaches the value of 365 nm, even for small ΔW. Consequently, the corresponding

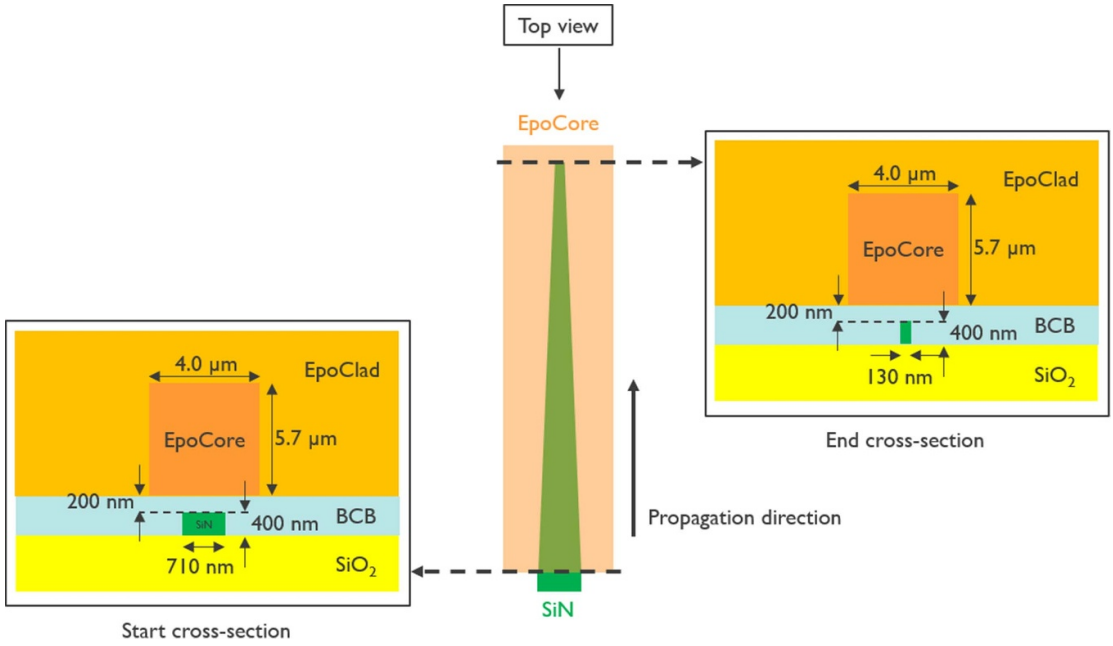

Figure 2. Schematic representation (images not to scale) of the SiN tapered waveguide, ranging from 710 nm to 130 nm width. The EpoCore waveguide dimensions do not change. For simplicity, the top view only shows the 2 waveguides.

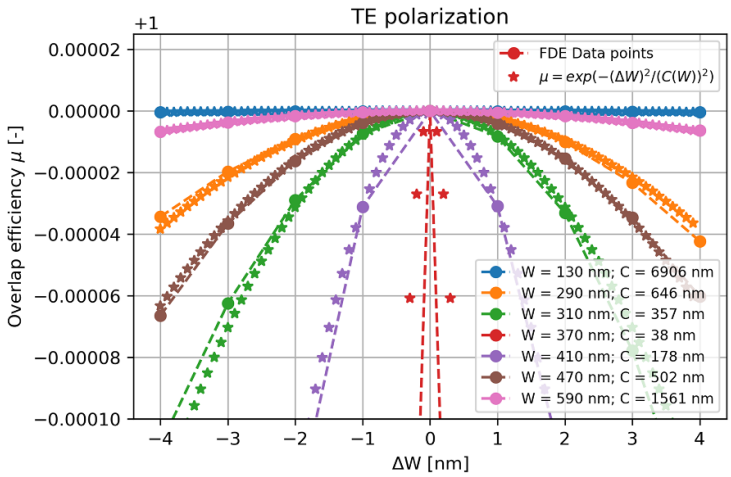

Figure 3. The overlap efficiency μ is shown for a few chosen W-values, as function of discrete steps ΔW, for the fundamental TE mode. Additionally, the fitted Gaussian profile is overlaid with a sampling resolution of 0.1 nm, relying on the calculated C(W) values.

Gaussian fit exhibits a narrow function, resulting in a low C-value for this specific width. Hence, the taper width should reduce more gradually to mitigate any significant intensity loss. This observation is reaffirmed in figure 4, which illustrates a local minimum for the C-value at $W = 365$ nm. To further analyze the data, a 16th order polynomial function is fitted to the Lumerical FDE data points for $C(W)$.

The significance of the $W = 365$ nm region in facilitating the coupling between both waveguides becomes more evident when examining the isolated TE/TM fundamental modes within the SiN tapered waveguide, as depicted in figure 5. In proximity to $W = 365$ nm, the effective index values of the fundamental TE/TM modes in the SiN waveguide closely align with those of the EpoCore's fundamental mode. Consequently, light within the SiN waveguide can be more readily coupled towards the EpoCore waveguide with minimal losses.

By incorporating the fit for $C(W)$ shown in figure 4 into equation (8), the resulting 'Mono' taper shape is depicted in figure 6. Initially, the taper width decreases rather fast with increasing z until $W \approx 450$ nm. Afterwards, the taper width evolves much slower, since $\alpha(W)$ is steadily rising with decreasing W, as

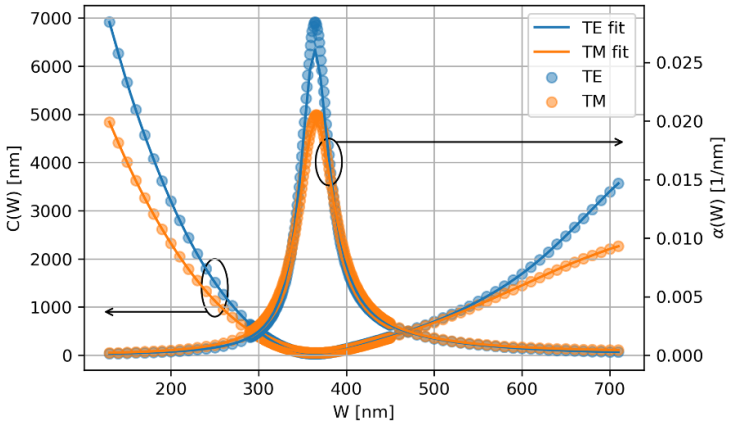

Figure 4. Behaviour for C and α as a function of W, for both the fundamental TE and TM modes. A 16th order polynomial function is used to represent a fitting of the Lumerical FDE data points. The minimal values for C(W) and maximal values for α(W) can be found in the region around W = 365 nm.

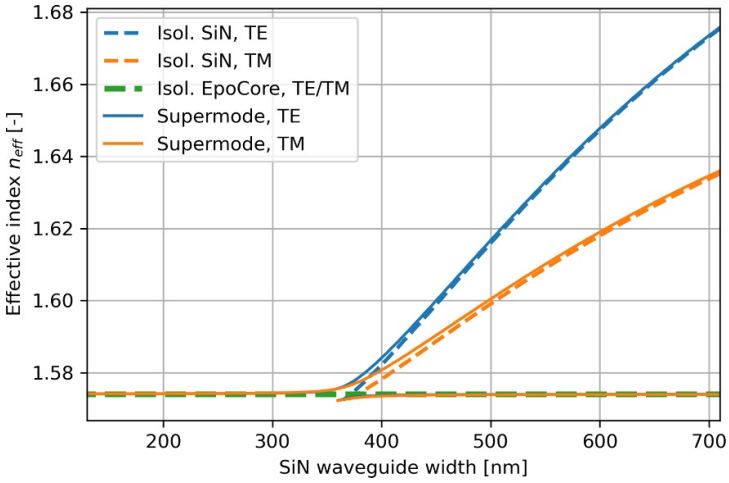

Figure 5. The effective index of the isolated fundamental TE and TM modes in the SiN tapered waveguide varies as function of the waveguide width W. The isolated EpoCore's fundamental TE/TM modes are independent of the SiN waveguide width and thus constant. The effective indices are almost identical in the region between W = 350 nm and W = 400 nm. When including both waveguides in the Lumerical FDE simulation, the displayed supermodes show the TE/TM modes' effective indices for varying SiN width.

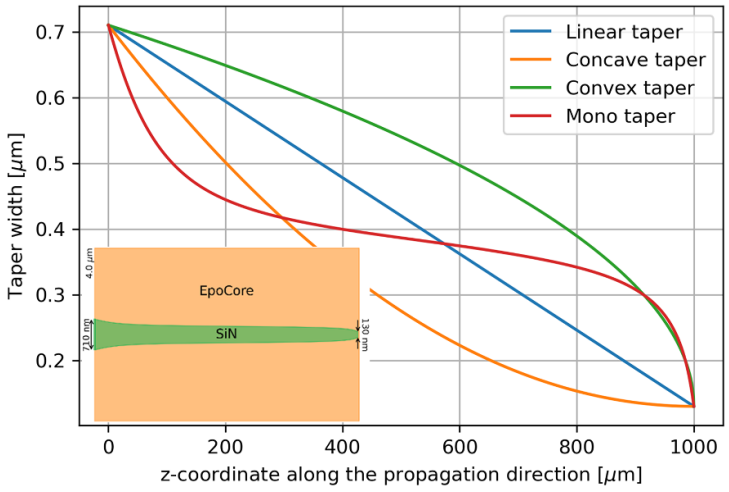

Figure 6. Depiction of a linear, concave, convex and 'Mono' taper shape as defined by equation (8), for a 1 mm long SiN taper. For simplicity, the horizontal axis shows the z-coordinate to better visualize the taper width variation along the propagation direction. The 'Mono' taper shape is the result for optimizing both fundamental TE and TM modes, with $\varepsilon = 1876\ m^{-1}$ for a taper length = 1 mm. The inset graphically shows the top view of the SiN 'Mono' taper and the EpoCore waveguide.

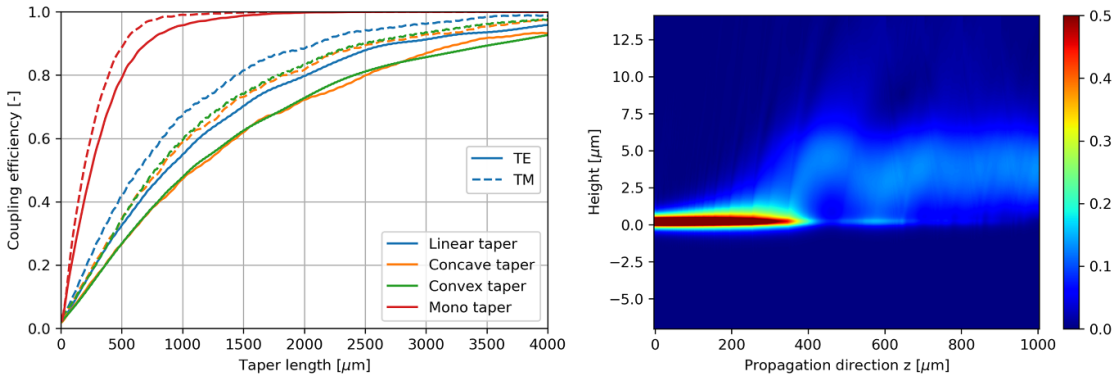

Figure 7. (left) Lumerical EME simulations compare the coupling efficiency for the linear, concave and convex taper with the 'Mono' taper, considering both TE and TM fundamental modes at $\lambda = 1310$ nm. (right) Lumerical 3D FDTD simulation to display the electric field distribution along the propagation direction z of the 'Mono' taper. The narrower the SiN taper, the more light is coupled to the upper polymer waveguide. The taper length is 1 mm and the simulation wavelength is 1308 nm.

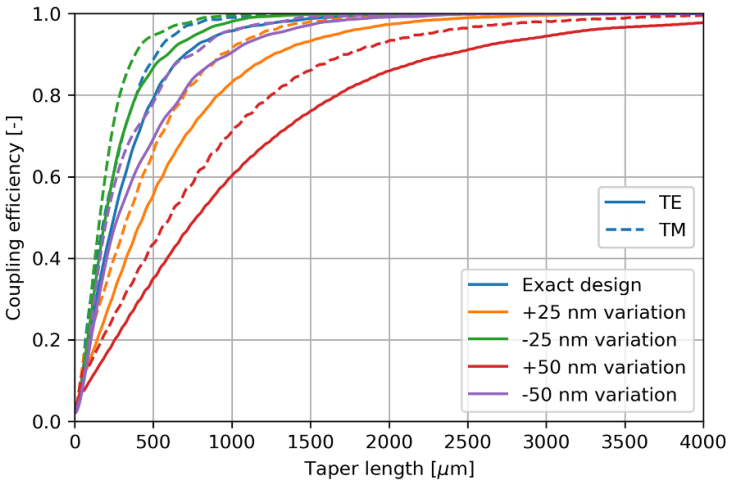

Figure 8. Lumerical EME simulation, analyzing the influence of a global width variation of the 1 mm long 'Mono' taper on the coupling efficiency, for both TE and TM polarizations at $\lambda = 1310$ nm.

indicated in figure 4. The maximum coupling occurs at W-values for which $\alpha(W)$ is maximal. When W decreases even more, $\alpha(W)$ becomes smaller again and the taper can evolve much faster, starting from $W \approx 310$ nm onwards. As comparison, figure 6 clearly depicts the different taper shape of the 'Mono' taper with respect to the more commonly used linear, concave and convex taper.

Initially, the scaling factor ε is arbitrarily chosen. After obtaining the 1-on-1 relationship between taper length z and taper width W and defining the desired total taper length, the value for ε can be changed accordingly. As such, this constant loss factor acts simultaneously as scaling factor to reshape the taper length.

As additional proof for the 'Mono' taper's functionality, figure 7 shows how the 'Mono' taper outperforms a linear, concave and convex taper in terms of coupling efficiency. Considering a taper length of 1 mm, the 'Mono' taper achieves 96% and 99% efficiency for TE and TM polarization respectively, which is on average an improvement of 40% compared to the other taper shapes. Besides this, the electric field distribution is displayed, showing the coupling from a compact SiN waveguide towards the broader polymer waveguide.

A final analysis is the influence of manufacturing tolerances of the configuration on the coupling efficiency. Since the taper shape can be subject to small changes due to manufacturing tolerances, figure 8 compares the exact design to its altered design with a global offset of ± 25 nm and ± 50 nm. For $+25$ nm, the coupling efficiency drops to 84% (TE) and 92% (TM) for a 1 mm long taper, while a variation of -25 nm even improves the efficiency up to 98% (TE) and 99.7% (TM). The latter result indicates a growing potential for adiabatic coupling if the minimal feature size for manufacturing is further enhanced. For $+50$ nm, the coupling efficiency drops even lower to 60% (TE) and 70% (TM), whereas a variation of -50 nm achieves

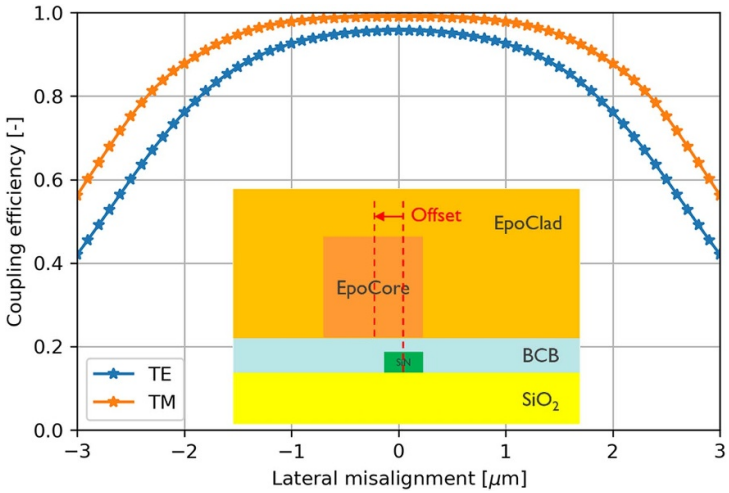

Figure 9. Lumerical EME simulation, showing the influence of lateral misalignment of the 1 mm long 'Mono' taper on the coupling efficiency, for both TE and TM polarizations at $\lambda = 1310$ nm. The inset graphically represents the offset in lateral direction.

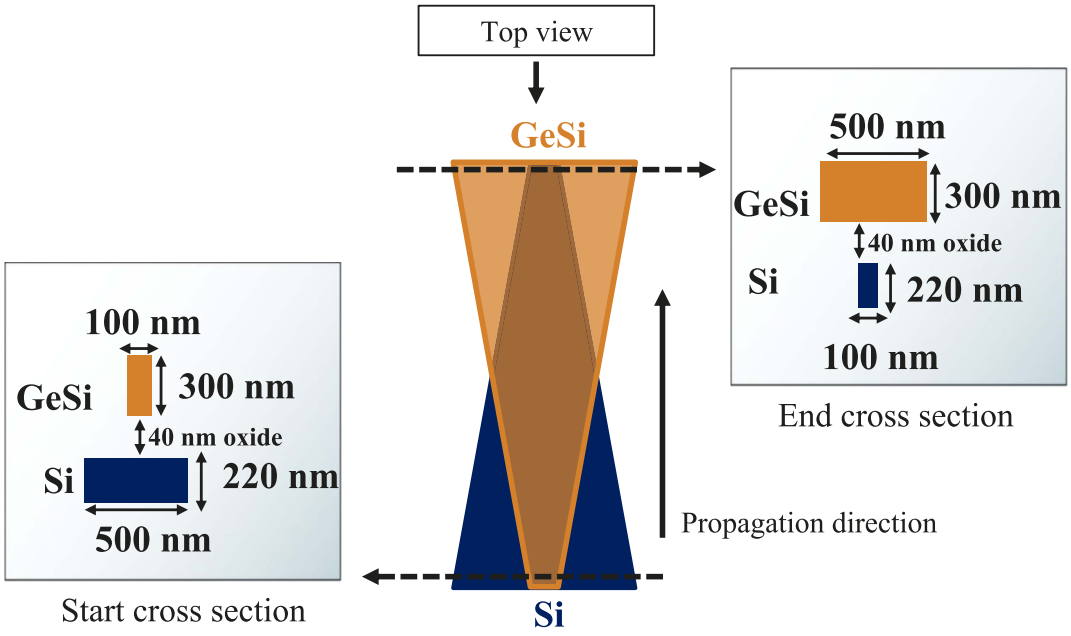

Figure 10. Schematic view of the start and end cross sections of the light coupling from the underlaying Si waveguide to the top GeSi waveguide. Separation silicon oxide layer of 40 nm is considered.

91% (TE) and 96% (TM). Next to that, figure 9 displays the influence of lateral misalignment of the EpoCore waveguide with respect to the SiN 'Mono' taper. In case of a misalignment equal to ± 2 μm, the coupling efficiency is reduced by 20%, hence an additional loss of 1 dB.

3.2. Si to GeSi coupling: double taper

As a second showcase, we consider light coupling between Si waveguide and GeSi waveguide used in the design of GeSi-based electroabsorption modulators and photodetectors [25, 26]. The two waveguides in this example are separated by 40 nm of Silicon oxide layer. The Si waveguide is tapered down from 500 nm to 100 nm in width, while the GeSi waveguide is tapered up from 100 nm to 500 nm in width. The waveguide height for Si and GeSi are respectively 220 nm and 300 nm, while their refractive index values are 3.5 and 4.16 at $\lambda = 1310$ nm. Figure 10 shows the start and end cross section schematics of the coupling between the two waveguides.

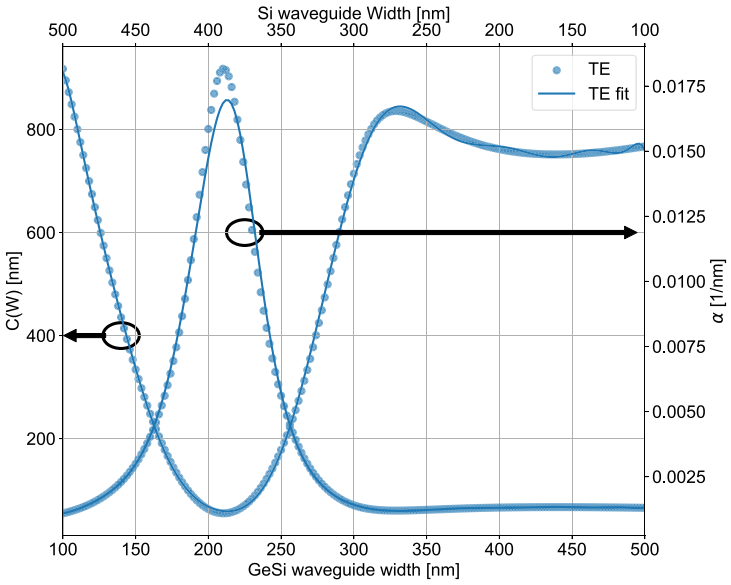

Figure 11. C(W) and α(W) as a function in the coupler cross section width, for both Si and GeSi waveguides. A polynomial function of order 16 was used to fit the data points. The minimum and maximum value of the polynomial functions occurs at GeSi width of ∼210 nm (Si width ∼390 nm) for the TE-mode, which corresponds to the phase matching point.

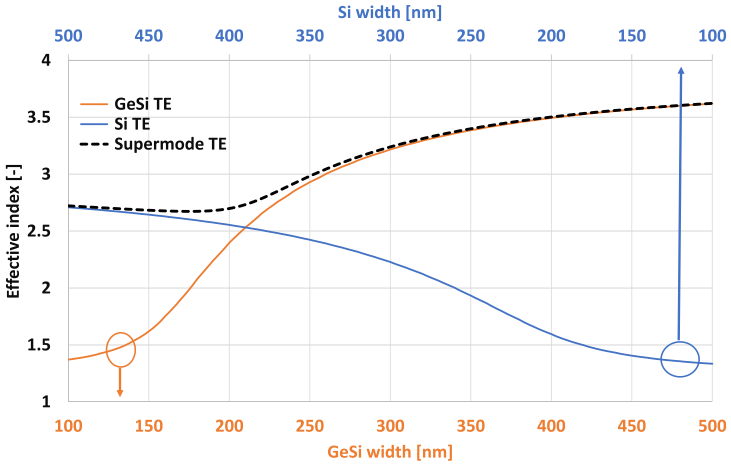

Figure 12. Calculated effective index of the fundamental TE-mode for GeSi waveguide (thickness = 300 nm), Si waveguide (thickness = 220 nm), and the first supermode (with GeSi and Si together) as a function of width. Phase matching point occurs at GeSi width of 210 nm and Si width = 390 nm with an effective index of 2.5314 at 1310 nm.

Following the same design flow of the previous example, we start by calculating the $C(W)$ and $\alpha(W)$ for different cross-sections along the propagation direction as indicated in figure 10. From the start until the end cross-section, the Si waveguide width consecutively decreases by 2 nm, while the GeSi waveguide width increases by 2 nm. For each cross-section, the overlap calculations are executed to extract the C-value as defined by equation (5). Figure 11 shows the calculated $C(W)$ data points at each cross section through which a polynomial function of order 16 is fitted, depicted as 'TE fit'. The $C(W)$ minimum value occurs at a GeSi width of 210 nm (Si width of 390 nm), which corresponds to the maximum value for $\alpha(W)$.

The $C(W)$ function behaviour can be explained by looking at the effective index of the waveguides to determine the phase matching condition. Figure 12 shows the calculated effective index for the fundamental TE-mode for both waveguides independently, as well as the effective index of the first supermode as a function of the different waveguide widths. In general, the effective index of a guided mode increases with increasing waveguide width. Since the GeSi waveguide is tapered up and the Si waveguide is tapered down, the effective index values for both waveguides become equal at GeSi width of 210 nm and Si width of

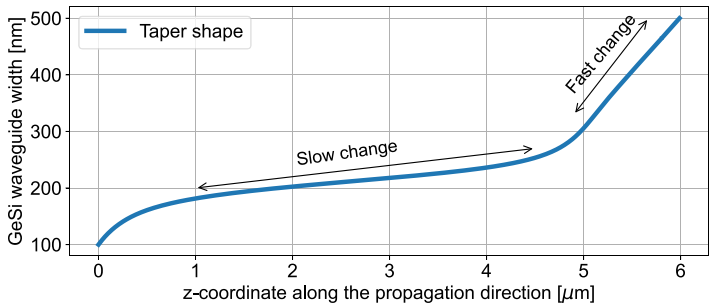

Figure 13. The generated taper shape by equation (8) (with $\varepsilon = 2.53 \times 10^5$ m^{-1}, results in taper length of 6 μm) using the polynomial function generated in figure 11 for the TE-mode. For better visualization of the taper shape, the y-axis is the taper width, and x-axis is the taper length along the propagation direction z.

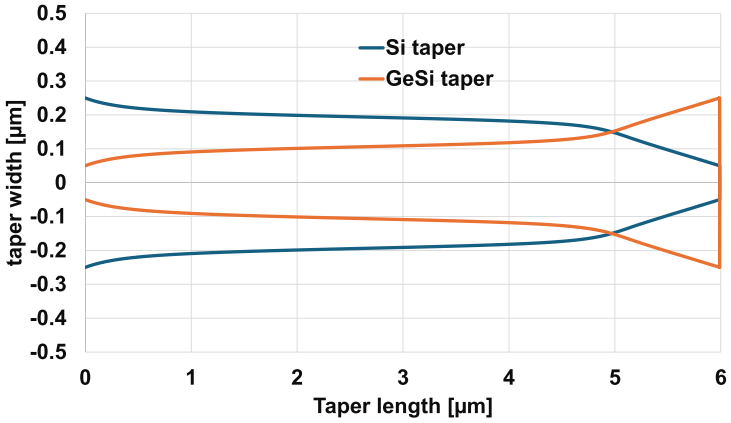

Figure 14. The tapers for both the Si and GeSi waveguides. Both tapers are generated using equation (8) (with $\varepsilon = 2.53 \times 10^5$ m^{-1}, results in taper length of ~6 μm) and the C(W) function in figure 11.

390 nm. For areas further away from the phase matching point, the supermode effective index is very close to the one of the individual Si or GeSi effective index as the mode is mostly confined in the corresponding waveguide. Around the phase matching point however, the supermode bridges the difference in effective index between both regions.

As expected, the phase matching point in figure 12 perfectly coincides with the minimum (maximum) of the $C(W)$ function ($\alpha(W)$ function) in figure 11. The taper shape function is then generated using equation (8). Using $\varepsilon = 2.53 \times 10^5$ m^{-1}, a taper length of 6 μm is generated and shown in figure 13. The characteristics of the $C(W)$ function are reaffirmed in the taper shape. For example, around the GeSi waveguide width of 210 nm (starting from ~190 nm to ~290 nm) the taper shape has a small slope (slow change) to meet the adiabaticity criterion. However, starting from GeSi waveguide width of ~290 nm, the taper function has a high slope (fast change) until it reaches the final width of 500 nm.

Figure 14 presents the two tapers of Si and GeSi. The GeSi taper starts from width of 0.1 μm and ends at width of 0.5 μm. On the other hand, the Si taper is tapered down from width of 0.5 μm and ends at taper tip of 0.1 μm. The two tapers are generated using equation (8) with the same $\varepsilon = 2.53 \times 10^5$ m^{-1}, such that they both have a length of 6 μm. The coupling performance of the tapers is then evaluated by Lumerical EME simulations and compared to its linear taper alternative. The coupling efficiency of the two cases is evaluated at wavelength of 1310 nm and plotted at figure 15. The 'Mono' taper of 6 μm has the same coupling efficiency of 98% as a 30 μm long linear and concave tapers, which is 5x reduction in length. Additionally, when compared to convex taper, the 'Mono' taper still demonstrates superior performance with ~2.2x reduction in length. Ansys Lumerical finite difference time domain (FDTD) simulation was used to show the coupling performance. Figure 16 (left) shows a side view of the coupling between the two waveguides, while

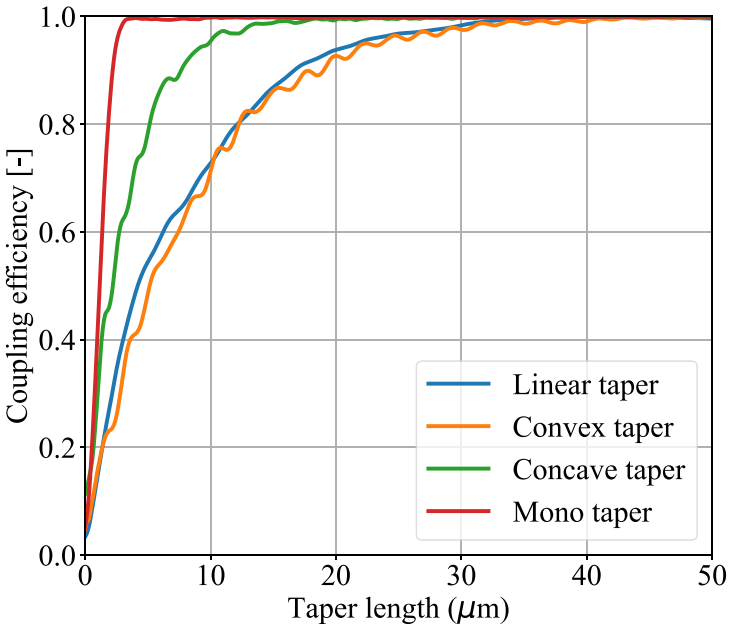

Figure 15. Comparison between the coupling efficiency for the proposed adiabatic taper with its linear, concave and convex taper alternatives at wavelength of 1310 nm.

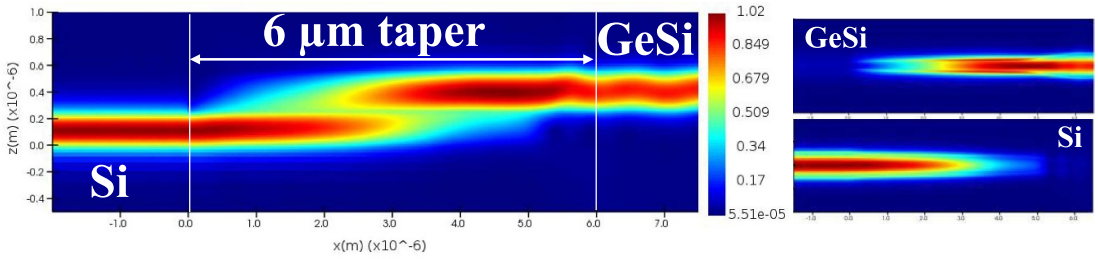

Figure 16. (left) Lumerical 3D FDTD simulation of the 6 μm adiabatic coupler performance at 1310 nm, with a coupling efficiency equal to 98%. (right) Top view of the field exchange between the Si and the GeSi waveguides.

figure 16 (right) depicts a top view of the field exchange between the Si and the GeSi waveguides using a horizontal monitor inside the two waveguides.

To assess the impact of fabrication errors and lateral misalignment on taper coupling performance, additional EME simulations were conducted. Figure 17 illustrates the coupling efficiency after applying width variations of $\pm$25 nm and $\pm$50 nm (as shown in the inset) to the taper design at a 1310 nm wavelength. For the 6 μm long 'Mono' taper, the coupling efficiency decreases to 97% and 95% for $+$25 nm and $-$25 nm variations respectively. A more significant reduction is observed with $\pm$50 nm variations, dropping the efficiency to 78% and 83%. However, this efficiency loss can be mitigated by increasing the taper length, as depicted in figure 17, with the final taper length choice depending on the anticipated fabrication errors. Additionally, the tolerance to lateral misalignment between the two tapers was examined. Figure 18 demonstrates that the coupling efficiency is $\sim$97% with a lateral misalignment of $\pm$100 nm.

4. Conclusion

We have presented a new, empirical model for designing adiabatic tapers. The 'Mono' method facilitates the design of adiabatic tapers for a broad range of applications, supporting heterogeneous integration of materials. The 'Mono' method depends on a bottom-up approach, in which we start by evaluating the C-value for all cross-sections along the propagation direction. The minimum of the $C(W)$ function is directly related to the phase matching point of problem of interest, which can optionally be verified by evaluating the effective index of the confined modes within the waveguides. Two examples were considered to showcase the taper design. The optimized SiN-to-polymer structure exhibits a 40% coupling improvement compared to a linear, concave and convex taper. The Si-to-GeSi adiabatic tapers of only 6 μm long result in a 5x reduction

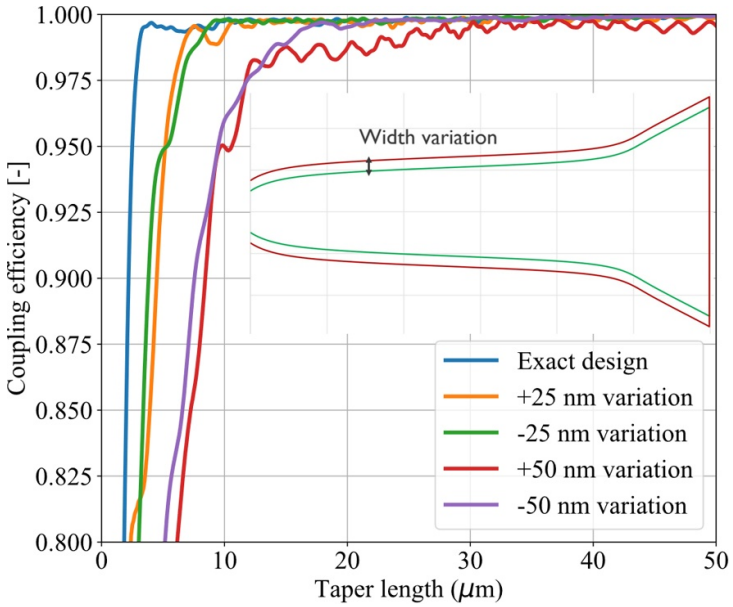

Figure 17. Lumerical EME simulation, showing the influence of fabrication error on the 6 μm long 'Mono' taper on the coupling efficiency for TE polarization at $\lambda = 1310$ nm.

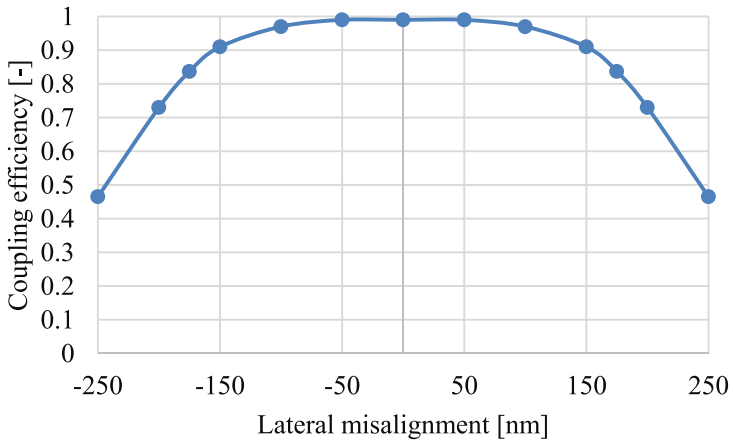

Figure 18. Lumerical EME simulation, showing the influence of lateral misalignment of the 6 μm long 'Mono' taper on the optical coupling loss, for TE polarization at $\lambda = 1310$ nm.

in length compared to the linear and convex taper alternatives, and a 2.2x length reduction compared to a concave taper. Besides this, this new proposed method has the advantages of easy calculations, enabling every photonic IC designer to directly generate the desired taper shape in two easy steps: Initially, the $C(W)$ function needs to be defined at different cross sections along the propagation direction of any problem of interest. Afterwards, the taper function can be generated with optimized coupling and reduced footprint.

Data availability statement

All data that support the findings of this study are included within the article.

Acknowledgments

Part of this work was supported by imec's industry-affiliation R&D Program on Optical I/O and by the European Union's Horizon Europe Research and Innovation Program under Agreement 101070560 (PUNCH).

ORCID iDs

Jef Van Asch https://orcid.org/0000-0002-0784-1131
Ahmed Kandeel https://orcid.org/0009-0005-0663-5714
Jeroen Missinne https://orcid.org/0000-0002-3470-620X
Peter Bienstman https://orcid.org/0000-0001-6259-464X
Dries Van Thourhout https://orcid.org/0000-0003-0111-431X
Geert Van Steenberge https://orcid.org/0000-0001-8574-1235
Joris Van Campenhout https://orcid.org/0000-0003-0778-2669

References

[1] Van Steenberge G *et al* Packaging of ultra-dynamic photonic switches and transceivers for integration into 5G radio access network and datacenter sub-systems *2023 IEEE 73rd Electronic Components and Technology Conf. (ECTC)* (https://doi.org/10.1109/ECTC51909.2023.00129)
[2] Pantouvaki M *et al* 2017 Active components for 50 Gb/s NRZ-OOK optical interconnects in a silicon photonics platform *J. Lightwave Technol.* **35** 631–8
[3] Kandeel A *et al* 2022 Low-capacitance, high-speed O-band GeSi quantum-confined stark effect electro absorption modulator *Frontiers in Optics + Laser Science 2022 (FIO, LS)* (*Technical Digest Series*) (Optica Publishing Group) p FTu6C.2
[4] Taillaert D, Bienstman P and Baets R 2004 Compact efficient broadband grating coupler for silicon-on-insulator waveguides *Opt. Lett.* **29** 2749–51
[5] Fischer U, Zinke T, Kropp J-R, Arndt F and Petermann K 1996 0.1 dB/cm waveguide losses in single-mode SOI rib waveguides *IEEE Photonics Technol. Lett.* **8** 647–8
[6] Galarza M, Van Thourhout D, Baets R and Lopez-Amo M 2008 Compact and highly-efficient polarization independent vertical resonant couplers for active-passive monolithic integration *Opt. Express* **16** 8350–8
[7] Shi Y, Kunert B, De Koninck Y, Pantouvaki M, Van Campenhout J and Van Thourhout D 2019 Novel adiabatic coupler for III–V nano-ridge laser grown on a Si photonics platform *Opt. Express* **27** 37781–94
[8] Bernson R *et al* Packaging strategies for 3D integration of photonic and electronic chips on a glass substrate *2023 IEEE 25th Electronics Packaging Technology Conf. (EPTC)* (https://doi.org/10.1109/EPTC59621.2023.10457729)
[9] Park S R and O B-H 2001 Novel design concept of waveguide mode adapter for low-loss mode conversion *IEEE Photonics Technol. Lett.* **13** 675–7
[10] Sun X, Liu H-C and Yariv A 2009 Adiabaticity criterion and the shortest adiabatic mode transformer in a coupled-waveguide system *Opt. Lett.* **34** 280–2
[11] Siriani D F and Tambasco J-L 2021 Adiabatic guided wave optics—a toolbox of generalized design and optimization methods *Opt. Express* **29** 3243–57
[12] Johnson S G, Bienstman P, Skorobogatiy M A, Ibanescu M, Lidorikis E and Joannopoulos J D 2002 Adiabatic theorem and continuous coupled-mode theory for efficient taper transitions in photonic crystals *Phys. Rev.* E **66** 066608
[13] Fu Y, Ye T, Tang W and Chu T 2014 Efficient adiabatic silicon-on-insulator waveguide taper *Photon. Res.* **2** A41–4
[14] Horth A, Cheben P, Schmid J H, Kashyap R and Quitoriano N J 2016 Ideal, constant-loss nanophotonic mode converter using a Lagrangian approach *Opt. Express* **24** 6680
[15] Mu J, Dijkstra M, Yong Y-S, Segerink F B, Wörhoff K, Hoekman M, Leinse A and García-Blanco S M 2017 Low-loss, broadband and high fabrication tolerant vertically tapered optical couplers for monolithic integration of Si_3N_4 and polymer waveguides *Opt. Lett.* **42** 3812–5
[16] Melikyan A and Dong P 2019 Adiabatic mode converters for silicon photonics: power and polarization broadband manipulators *APL Photonics* **4** 030803
[17] Ng V, Tuniz A, Dawes J M and de Sterke C M 2019 Insights from a systematic study of crosstalk in adiabatic couplers *OSA Contin.* **2** 629–39
[18] Chung H-C, Martínez-Garaot S, Chen X, Muga J G and Tseng S-Y 2019 Shortcuts to adiabaticity in optical waveguides *Europhys. Lett.* **127** 34001
[19] Evangelakos V, Paspalakis E and Stefanatos D 2023 Efficient light transfer in coupled nonlinear triple waveguides using shortcuts to adiabaticity *Sci. Rep.* **13** 1368
[20] Overlap analysis-Ansys Lumerical (available at: https://optics.ansys.com/hc/en-us/articles/360034917453-Overlap-analysis-Modal-Analysis-Tab)
[21] Sacher W D, Huang Y, Ding L, Barwicz T, Mikkelsen J C, Taylor B J F, Lo G-Q and Poon J K S 2014 Polarization rotator-splitters and controllers in a Si_3N_4-on-SOI integrated photonics platform *Opt. Express* **22** 11167–74
[22] Van Asch J *et al* 2024 Sub-1 dB loss SiN-to-polymer waveguide coupling: an enabler for co-packaged optics *2024 Optical Fiber Communications Conf. and Exhibition (OFC)* (*San Diego, CA, USA*) pp 1–3 (available at: https://ieeexplore.ieee.org/document/10526782)
[23] Van Asch J *et al* 2022 Design of a broadband adiabatic coupler for interfacing PICs to optical redistribution layers *IEEE Benelux Photonics Chapter: Annual Symp. 2022, Proc.* (*Eindhoven, the Netherlands*)
[24] Micro Resist Technology GmbH datasheet (available at: www.microresist.de/en/produkt/epocore-epoclad-series/)
[25] Li Y and Cheng B 2013 Efficient evanescent coupling design for GeSi electro-absorption modulator *Chin. Phys.* B **22** 124209
[26] Zhou H, Sun J, Gao J, Jiang J and Zhou Y 2016 Design of compact and efficient polarization-insensitive taper coupler for SiGe photonic integration *Opt. Express* **24** 23784–97